Circulation of Pacific Winter Water in the Western Arctic Ocean

Wenli Zhong[1,2] (iD), **Michael Steele[2]** (iD), **Jinlun Zhang[2]** (iD), and **Sylvia T. Cole[3]** (iD)

[1]Key Laboratory of Physical Oceanography, Ocean University of China, Qingdao, China, [2]Applied Physics Laboratory, University of Washington, Seattle, WA, USA, [3]Woods Hole Oceanographic Institution, Woods Hole, MA, USA

Abstract Pacific Winter Water (PWW) enters the western Arctic Ocean from the Chukchi Sea; however, the physical mechanisms that regulate its circulation within the deep basin are still not clear. Here, we investigate the interannual variability of PWW with a comprehensive data set over a decade. We quantify the thickening and expansion of the PWW layer during 2002–2016, as well as its changing pathway. The total volume of PWW in the Beaufort Gyre (BG) region is estimated to have increased from $3.48 \pm 0.04 \times 10^{14}\,\mathrm{m}^3$ during 2002–2006 to $4.11 \pm 0.02 \times 10^{14}\,\mathrm{m}^3$ during 2011–2016, an increase of 18%. We find that the deepening rate of the lower bound of PWW is almost double that of its upper bound in the northern Canada Basin, a result of lateral flux convergence of PWW (via lateral advection of PWW from the Chukchi Borderland) in addition to the Ekman pumping. In particular, of the 70-m deepening of PWW at its lower bound observed over 2003–2011 in the northwestern basin, 43% resulted from lateral flux convergence. We also find a redistribution of PWW in recent years toward the Chukchi Borderland associated with the wind-driven spin-up and westward shift of the BG. Finally, we hypothesize that a recently observed increase of lower halocline eddies in the BG might be explained by this redistribution, through a compression mechanism over the Chukchi Borderland.

Plain Language Summary Pacific Winter Water (PWW) is a deeper freshwater source via subduction in contrast to the wind-driven Ekman convergence of freshwater in the surface Ekman layer of the western Arctic Ocean. It supplies the western Arctic Ocean with acidifying water. Our study reveals a redistribution of PWW associated with the wind-driven spin-up of Beaufort Gyre. The lateral advection of PWW from the Chukchi Borderland to the northern Canada Basin plays an important role in the deepening of PWW lower bound at the edge of Beaufort Gyre. In addition, the total volume of PWW has increased about 18% over the years 2002–2016. Our findings provide an important implication not only for the physical oceanographer but also for the marine chemists and biologists.

1. Introduction

In the western Arctic Ocean, the cold and relatively fresh Pacific Winter Water (PWW) lies above the warm and salty Atlantic Water (AW). The PWW could be referred to as a type of cold halocline water because of its relatively cold temperature (Aagaard et al., 1981; Coachman et al., 1975; Shimada et al., 2005; Timmermans et al., 2017). The variability of cold halocline water has a great impact on the vertical heat transfer from the AW to the upper ocean and the sea ice (Lique et al., 2014; Shimada et al., 2005; Steele & Boyd, 1998; Woodgate, Aagaard, Swift, et al., 2005). The PWW is a high nutrient and low dissolved oxygen water (Codispoti et al., 2005; Jones & Anderson, 1986; Woodgate, Aagaard, Swift, et al., 2005) that supplies the western Arctic Ocean with acidifying water, which is reported to have expanded in the western Arctic Ocean in recent years (Qi et al., 2017). The water properties of PWW are determined by the inflow of Pacific water through Bering Strait in winter and by ice-ocean processes (e.g., brine rejection) in the Chukchi Sea (Itoh et al., 2012; Melling, 1993; Melling & Lewis, 1982; Shimada et al., 2005; Weingartner et al., 1998; Woodgate & Aagaard, 2005; Woodgate, Aagaard, Swift, et al., 2005). It then ventilates the lower halocline of the deep Canada Basin either by lateral injection or by diapycnal mixing with the AW below (Woodgate, Aagaard, Swift, et al., 2005). Itoh et al. (2012) studied the interannual variability of PWW formation by investigating the connection between the upstream in the northeastern Chukchi Sea and Barrow Canyon and the downstream in the Canada Basin (Figure 1). Their results indicate the important role of Alaskan coastal polynyas in regulating the interannual variability of PWW.
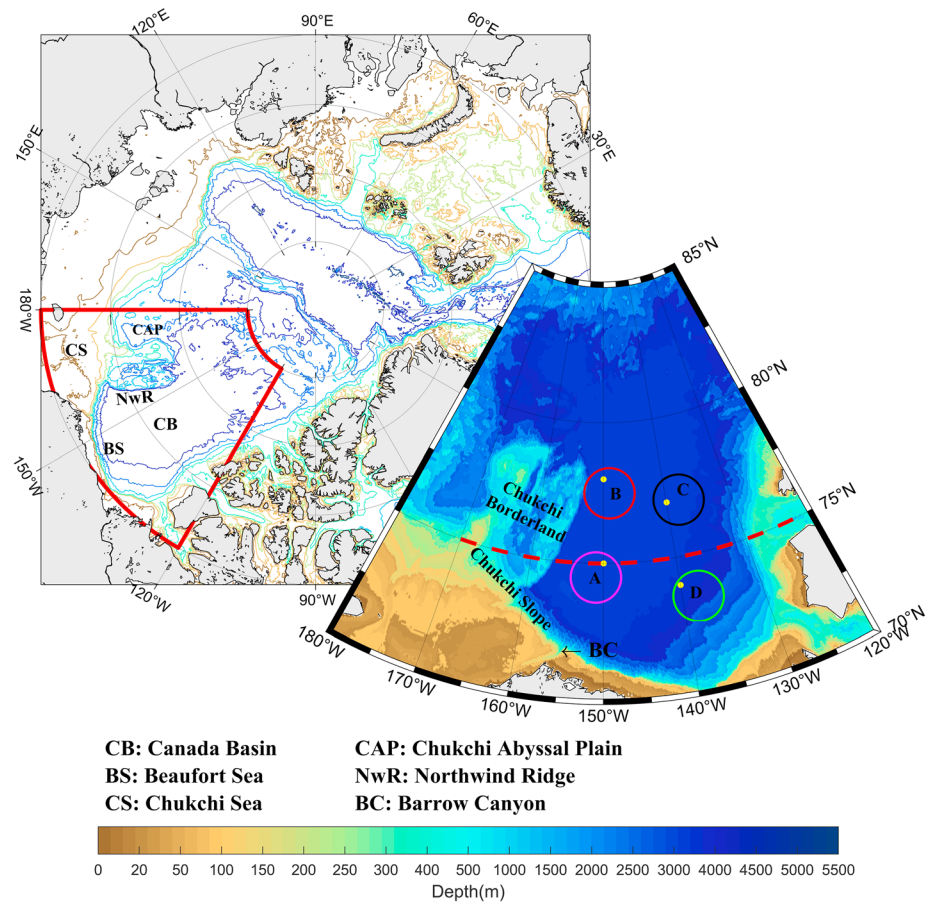
Figure 1. The bathymetry of the western Arctic Ocean from IBCAO-v3 data (Jakobsson et al., 2012). The locations of four Beaufort Gyre Observing System (BGOS) moorings are marked as the yellow dots. The red dashed line marks the zonal section in Figure 2. The colored circles are used for the regional averaging for Figures 3 and 4, each with a radius of 100 km.

Pacific Summer Water (PSW), which lies directly above PWW, subducts in the Chukchi Sea and circulates in the Canada Basin in response to the wind-forced Beaufort Gyre (BG), following an anticyclonic helical pathway (Steele et al., 2004; Timmermans et al., 2014, 2017). In contrast, the pathway of PWW is seldom addressed and it is unclear to what extent the PWW is directly influenced by the wind forcing. Although modeling studies have shown an anticyclonic pathway of the Pacific water in the western Arctic Ocean (e.g., Aksenov et al., 2011, 2016; Timmermans et al., 2014, 2017), the general basin-scale PWW pathway in the western Arctic Ocean from observation and its response to the spin-up of the BG in recent years have yet to be addressed. Here, the BG spin-up is also referred to as the intensification of the geostrophic current in the BG region (e.g., Armitage et al., 2017; McPhee, 2013).

Studies have revealed a westward movement of the BG in recent years (Armitage et al., 2017; Zhong et al., 2018) and an increase of eddy activity in the western Canada Basin (Armitage et al., 2017; Zhao et al., 2016). Zhao et al. (2016) showed a dramatic increase of lower halocline mesoscale eddies (having core salinities ≳32 and core depths ≳80 m) in recent years but not the upper halocline mesoscale eddies (having core salinities ≲32 and core depths ≲80 m). Armitage et al. (2017) hypothesized that eddies with a surface signature have increased via an interaction between the BG and steep topography, although the specific physical processes were not explored. Wind-driven Ekman pumping has a close connection with the eddy activity (Manucharyan & Spall, 2016; Yang et al., 2016; Manucharyan et al., 2016), but recent studies indicate that the maximum Ekman pumping is not in the BG center but rather in the Chukchi Sea (Dewey et al., 2018; Meneghello et al., 2018; Zhong et al., 2018). In addition, while there was no significant increasing trend of Ekman pumping in the BG during 2002–2014 (Zhang et al., 2016; Zhong et al., 2018), the geostrophic current and sea ice speeds both show significant increasing trends during this period (Zhong et al., 2018). On the other hand, several studies have revealed the important role of eddies in mediating the spin-up of the BG and

stabilizing halocline deepening in recent years (e.g., Manucharyan & Spall, 2016; Manucharyan et al., 2016; Meneghello et al., 2017; Yang et al., 2016). The different variability of lower halocline eddies compared with upper halocline eddies revealed in Zhao et al. (2016) suggests that something beyond a direct wind-driven process might be important in this partition and this requires further investigation.

In this study, we will address these issues by studying the characteristics and changing pathway of PWW in the western Arctic Ocean and its potential influences, using comprehensive in situ hydrographic and mooring data from 2002 to 2016. The PWW is ventilated through the mixed layer in the Chukchi Sea in winter (Timmermans et al., 2017; Woodgate, Aagaard, & Weingartner, 2005) and subducts along its corresponding isopycnals into the basin. The exact place of this subduction in the Chukchi Sea is still an ongoing research issue. But this is not the focus of our study here. Instead, we focus on the downstream effects of the changing pathway of PWW and the inflation of the PWW layer. Section 2 describes the data and methods. Section 3 shows the interannual variability of PWW and its corresponding influences. Summary and discussion are given in section 4.

2. Data and Methods

2.1. Data

In situ hydrographic data from a variety of sources over the years 2002–2016 are used for our analysis. Part of the hydrographic data is from the Unified Database for Arctic and Subarctic Hydrography (UDASH) version 1.0 (Behrendt et al., 2018). The UDASH is a unified and high-quality temperature and salinity data set for the Arctic Ocean and subpolar seas, thoroughly quality checked to remove duplicate and erroneous profiles (Behrendt et al., 2018). We also used more recent conductivity-temperature-depth data collected from (1) the Beaufort Gyre Exploration Project (BGEP) at the Woods Hole Oceanographic Institution, in collaboration with researchers from Fisheries and Oceans Canada at the Institute of Ocean Sciences (http://www. whoi.edu/website/beaufortgyre/); (2) the Japan Agency for Marine–Earth Science and Technology (JAMSTEC, http://www.godac.jamstec.go.jp/darwin/); (3) the Chinese Arctic Research Expedition (http:// www.chinare.org.cn); (4) the USCGC Healy (Swift, 2017); and (5) the Ice-Tethered Profiler (ITP) over September 2004 to October 2012 (the fully processed level 3 data). The ITP measures the pressure, temperature, and salinity between ~7 and ~750 m. Detailed processing procedures of ITP data can be found at http:// www.whoi.edu/itp. All the in situ hydrographic profiles here are linearly interpolated into 1-m vertical bins. Although our main focus here is the PWW, it is difficult to construct spatial winter fields from these hydrographic data due to a lack of observations during this season. Thus, the hydrographic data used here are restricted to July–October of each year to remove the seasonal variability.

The data are optimally interpolated onto a regular grid with a grid spacing of 0.5° in longitude and 0.1° in latitude, using the Data-Interpolating Variational Analysis (DIVA) (Troupin et al., 2012). The poor man's estimate method (error estimates derived by analyzing a vector of *covariances* with constant background field variance) is used to calculate the relative error fields, which are scaled by the local variance of the background field. Relative interpolation errors larger than 80% (15%) are masked for annual (multiyear) gridded maps. A 2-D spatial boxcar filter for smoothing (the length scale for smoothing is 3° in longitude and 0.6° in latitude) is applied to the gridding maps.

Data from four Beaufort Gyre Observing System (BGOS) moorings are also used for analyzing the seasonal and interannual variability of PWW (mooring locations shown in Figure 1). Each mooring is equipped with a McLane Moored Profiler (MMP) that measures conductivity, temperature, depth, and velocity. The MMP profiles span a depth range of ~50 to 2,000 m and are alternately separated in time by 6 and 48 hr (Proshutinsky et al., 2009). The final processed data have a 2-m vertical resolution. Potential density derived from the Polar Hydrographic Climatology ocean data (1° × 1°; PHC 3.0; Steele et al., 2001) is used as the reference field to study the perturbation of PWW from pre-2002 data, while the Monthly Isopycnal/Mixed-layer Ocean Climatology (MIMOC) data (Schmidtko et al., 2013) are used to represent the climatology field during 2002–2011.

2.2. Methods

In contrast to some previous studies, which define PWW by a salinity range centered on 33.1 (Itoh et al., 2012; Proshutinsky et al., 2011), the PWW here is defined as the water bounded by the isopycnals of 26
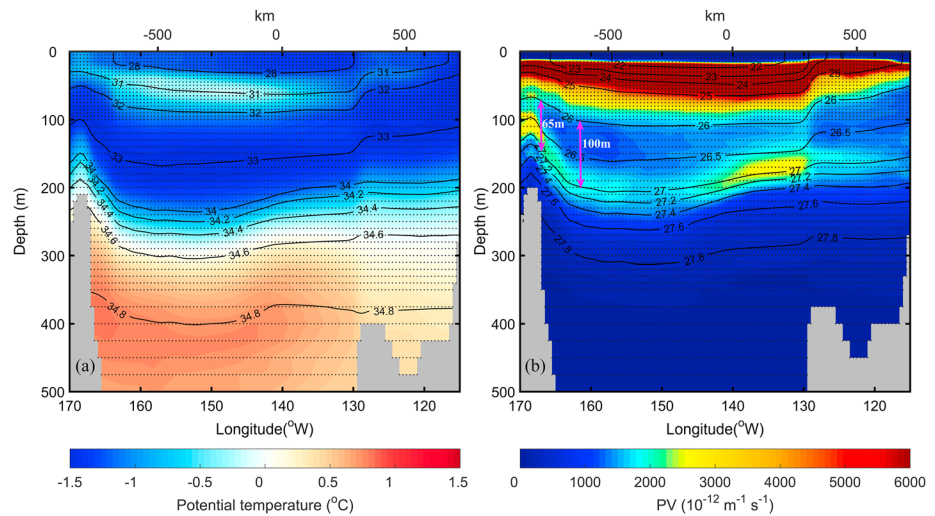
Figure 2. Sections of (a) potential temperature (shading) and salinity (contour), (b) potential vorticity (shading) and potential density (contour) along 75°N from Monthly Isopycnal/Mixed-layer Ocean Climatology (MIMOC) data (location of the section is shown in Figure 1). The black dots are the gridded points of MIMOC data. The pink double arrows in (b) represent the thickness of the Pacific Winter Water (PWW) layer at different locations.

and 27 kg/m^3 (Figure 2). This choice is generally consistent with the winter-transformed water property at the Barrow Canyon source region of PWW (Pickart et al., 2005) and brackets a layer of low potential vorticity (PV) water in the western Arctic Ocean where the salinity of 33.1 is also included (see also Nishino et al., 2008).

Here, PV is defined as $Q = -(f/\rho)\partial\sigma/\partial z$, where ρ is the in situ density, σ is the potential density, and f is the Coriolis parameter. Our definition here is a simplified form of the Ertel PV; that is, only the stretching vorticity term is considered (also see Pickart et al., 2005). The relative vorticity and tilting vorticity are assumed to be small, which is reasonable since we only consider the large-scale circulation in the western Arctic Ocean. We will show in section 3.1 that the PV analysis could also be framed as an analysis of isopycnal layer thickness and volume. We adopted the PV framework, which can be used as a passive circulation tracer (e.g., Maze & Marshall, 2011) to study the pathway of PWW.

To analyze the circulation of PWW, we use the Montgomery stream function, which traces geostrophic flow on surfaces of constant density anomaly (Aksenov et al., 2011; McDougall, 1989). The dynamical relationship between the PV Q and the Montgomery function has been discussed in detail in Marshall et al. (2001), Aksenov et al. (2011), and Maze and Marshall (2011). We refer the readers to these papers for details. Here we consider the large-scale steady circulation of PWW, and in this case the Rossby number is reasonably assumed to be small. So the Montgomery function M is also a stream function for layer-integrated PV flux, which helps us to diagnose the PV fluxes (Aksenov et al., 2011). Note that this may not be the case for flows over the shelf break as they could be strong, that is, with a relatively large Rossby number. The Montgomery function M is formulated as (McDougall, 1989)

$$M = p\delta - \int \delta \mathrm{d}p \tag{1}$$

where p is pressure and δ is the specific volume anomaly. The in situ hydrographic data described in section 2.1 are used to calculate the Montgomery function. The 2-D spatial boxcar filter is applied to smooth the gridding maps of multiyear mean Montgomery function and PV to remove/reduce the effects from mesoscale eddies, as we focus on the general circulation.

In this study, we calculate the freshwater budgets of the PWW layer and the upper 50 m. The freshwater content is defined as $\mathrm{FWC} = \int_{h_2}^{h_1} [S_{\mathrm{ref}} - S(z)]/S_{\mathrm{ref}} \mathrm{d}z$, which is integrated between the upper bound h_1 and lower bound h_2 of the corresponding water masses. The reference salinity is $S_{\mathrm{ref}} = 34.8$ (e.g., Proshutinsky et al., 2009).

The influence of the changing pathway of PWW on the structure of the cold halocline is considered here by calculating the eddy available potential energy (EAPE). The computation of EAPE differs from the

computation of time-mean available potential energy as it requires no complex reference state or background potential energy and instead relies upon a locally calculated mean-isopycnal state (Luecke et al., 2017). This quantity is a function of both background stratification and isopycnal fluctuations, and it indicates the energy of fluctuations in density around a time mean. The EAPE is given by (Luecke et al., 2017)

$$\text{EAPE} = \frac{g^2 \rho'^2}{2\rho_0^2 N^2} \tag{2}$$

where g is the gravitational acceleration, ρ' is the departure of in situ potential density relative to the PHC climatology potential density (climatology mean in July–October), ρ_0 is a reference density, and N^2 is the buoyancy frequency. The EAPE here contains both mesoscale and lower-frequency energy.

3. Results

Figure 2 shows a distinct vertical structure of the water masses in the Canada Basin. The relatively warm and highly stratified PSW is at a depth of ~50 m. The cold PWW lies below the PSW and above the warm and salty AW (that lies at ~400 m). The stratification is relatively strong between the PWW and the AW, with a PV of $\sim 2 \times 10^{-9} \cdot \text{m}^{-1} \cdot \text{s}^{-1}$. The core of PWW is represented by the isopycnal of 26.5 kg/m³ here, while the isopycnals of 26 and 27 kg/m³ (i.e., the upper and lower bounds of PWW) could be represented as the upper halocline and lower halocline, respectively (with relatively strong PV). Here, we focus on the multiyear changes of the PWW layer using the new definition of PWW in the following sections.

3.1. Multiyear Changes of PWW From Hydrographic and Mooring Data

We have defined the PWW in terms of its density with specific density surfaces chosen based on the general vertical PV structure. Depressions of the isopycnals are a combined effect of wind forcing (i.e., Ekman convergence) and the volumetric injection of PWW from the Chukchi Sea (Shimada et al., 2005), which is also referred to as subduction in Timmermans et al. (2014, 2017). To investigate these distinct processes further, the in situ hydrographic data are interpolated onto the regular grids using the DIVA method described in section 2.1. Note that the mooring data are not incorporated into the grids here. We then define four circular regions (each with a radius of 100 km) located at the four corners of our area of interest (see Figure 1). These four regions are defined based on a consideration to better represent the spatial variability of PWW around the basin (similar to the consideration for the mooring locations). The PWW upper bound behaves quite similarly at all four regions over time, with an overall deepening of ~30 m that seems to have stabilized since 2008 (Figure 3a). The position of the deepest upper bound of PWW is consistent with the position of the maximum freshwater content in the upper 50 m (not shown). This indicates that the upper PWW bound is strongly influenced by the Ekman convergence of freshwater in the Ekman layer; that is, the deepening of isopycnal 26 kg/m³ is a direct consequence of the accumulation of freshwater above it. In contrast, the variability of the PWW lower bound is very different among the four regions and seems to have no correlation with the overlying Ekman layer freshwater content. The largest depth increase of the lower bound (~70 m) occurs in the northwestern and northeastern regions.

The different deepening rates of the upper and lower PWW bounds lead to a significant increase of PWW layer thickness in the northwestern/northeastern regions since 2005/2008 (Figure 3b). On the other hand, the upper and lower bounds in the southwestern region increase at a comparable rate, resulting in a relatively stable thickness over the years 2002–2016. While the thickness change in the southeastern region is determined largely by the upper bound, which decreases in 2005–2009 and then increases in 2009–2011. The PWW thickness variability is highly correlated with its freshwater content variability (solid-dotted line and dashed-dotted line), which shows an interesting time-lagged onset of increased values from the northwestern (2005) to the northeastern (2008) and finally to the southeastern (2009) regions. In addition, the thickness and freshwater content in the PWW layer in all regions reach a similar plateau after their increase. We will discuss this further in the following sections.

All regions in our hydrographic analysis show a general warming of potential temperature minima in the PWW layer during 2002–2016 (Figure 4), with a time lag similar to that seen for layer thickness and freshwater content. In the two northern regions, a distinct temperature maximum over the PWW denotes summer Bering Sea Water (Steele et al., 2004; Timmermans et al., 2014), which was absent after ~2009, likely
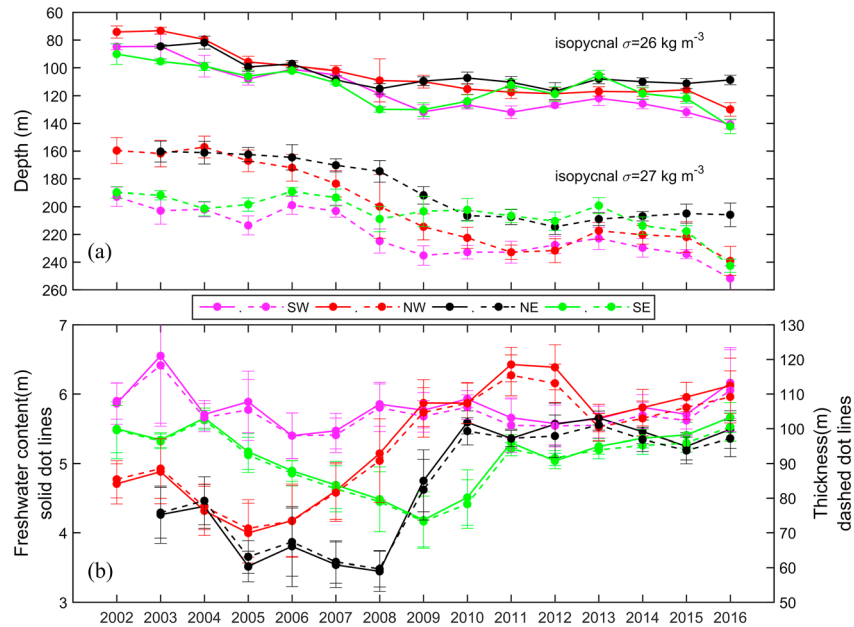
Figure 3. Regional averages of (a) depth of isopycnals 26 kg/m³ (solid line) and 27 kg/m³ (dashed line) and (b) the freshwater content relative to the salinity of 34.8 (solid-dotted line) and thickness of the PWW layer (dashed-dotted line). For each region, the interpolated fields are averaged within a radius of 100 km (grid cells with relative interpolation errors larger than 80% were removed and each region with 60 or more valid grid cells are used for analysis). The error bar indicates plus or minus one standard deviation of the variables in the defined region. The abbreviations *SW*, *NW*, *NE*, and SE are represented as the southwestern, northwestern, northeastern, and southeastern regions, respectively (regions shown as color circles in Figure 1). The corresponding spatial maps of (a) and (b) are shown in Figures S1 and S2 and S3 and S4, respectively.

related to spatial shifts of this water mass. The pulse-like signals of PWW advection (relatively warm and cold PWW minima alternate during years) seen in the two northern and southeastern regions are consistent with the north-eastward progression of the water mass that was discussed in Timmermans et al. (2014). Another source of PWW temperature change might be thermohaline intrusion from the underlying warm AW, but this is likely a small effect, owing to the strong stratification between AW and PWW (Lique et al., 2014; McLaughlin et al., 2009). We will show in section 3.2 that the pulse-like signals of temperature changes in PWW are related to the lateral advection of PWW from the Chukchi Borderland.

We now turn to mooring data to perform a similar analysis, but with higher temporal resolution and more details. Figure 5 shows a general deepening of the upper and lower PWW bounds, with noticeably different deepening rate of the two bounds at mooring B. Cold halocline mesoscale eddies are frequently captured by the moorings, and they strongly change the vertical structure of the PWW layer (e.g., January 2015 at mooring D). On the other hand, the deep mesoscale eddies with their cores at the depth of ~1,200 m (Carpenter & Timmermans, 2012) likely have only a small effect on the PWW layer.

We applied a 1-month boxcar filter to the time series in Figure 5 and examined some characteristics of PWW (Figure 6). This timescale of the filter will smooth out much of mesoscale eddies signals (Zhao et al., 2016) but maintain the fluctuations longer than 1 month (Meneghello et al., 2017), which we will consider as lateral eddy flux in section 3.3. The average PV in the PWW layer has a significant negative correlation with the PWW thickness at the four moorings (Figure 6, left panels, and Figure S5 in the supporting information). In addition, the extrema of PWW thickness are linked to the extrema of velocity, suggesting that some types of eddies (mesoscale eddies identified by Zhao et al., 2016, and/or larger-scale fluctuations) are prevalent in the PWW layer. Anticyclonic mesoscale eddies from the edges of the BG would elevate/depress the local upper bound/lower bound of PWW, resulting in PWW layer thickening. However, we cannot determine if the mesoscale eddies are passing through the moorings or if they are formed locally from baroclinic instability. Also, an annual thickening of the PWW layer is seen at moorings B and C around January in 2006 and 2007, accompanied by lower PV and relatively small velocity (<10 cm/s). These relatively weak velocities in
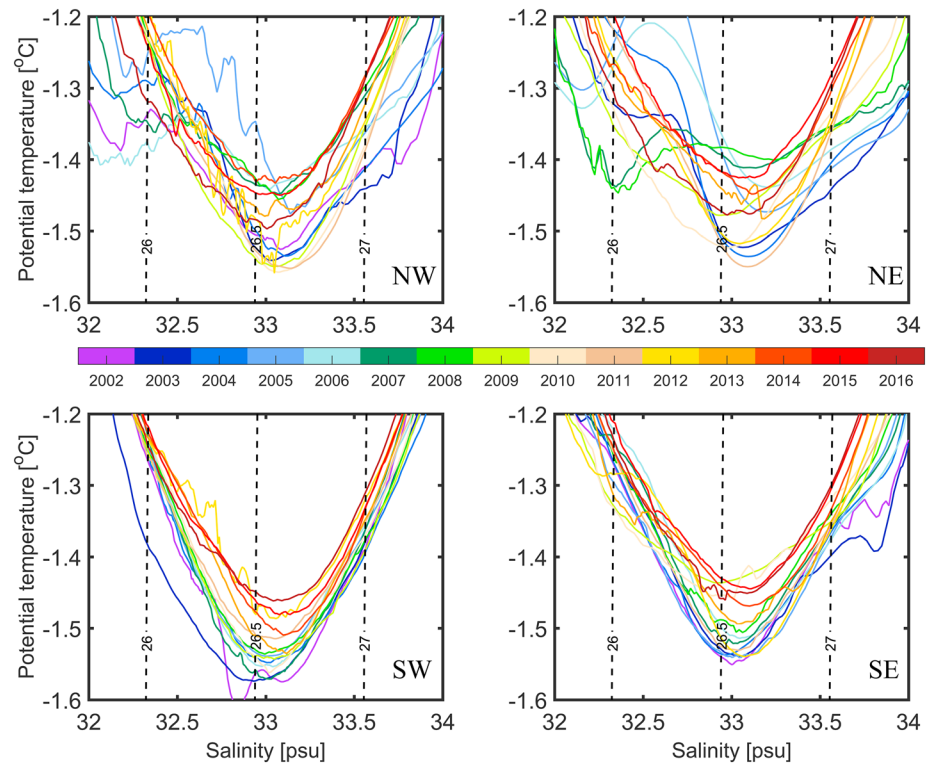
Figure 4. Regional potential temperature versus salinity in the Pacific Winter Water (PWW) layer from the original conductivity-temperature-depth (CTD) profiles during 2002–2016. The abbreviations *SW*, *NW*, *NE*, and *SE* are the same as in Figure 3. Note that no profiles are available in the northeastern region in 2002.

particular suggest that these signals arise from large-scale advection (which is relatively slow), rather than from mesoscale eddies (which have faster speeds). Further, the thickness of the PWW layer at moorings B and C has a significant negative correlation coefficient with the potential temperature in contrast to that at moorings A and D (Figure S5), suggesting that colder temperature is associated with the thickening of the PWW layer induced by the advection of PWW. The potential temperature at mooring A shows a gradual increase of ~0.1 °C over the years (Figure 6, right panels), while that of the other moorings show pulse-like signals. This is consistent with the results shown in Figure 4.

A summary of the deepening rates of isopycnals 26 and 27 using both hydrographic and mooring data is presented in Table 1 (linear fit of the annual mean values). The deepening rates estimated from these two kinds of data are generally consistent with each other. The largest difference of the deepening rate between isopycnals 26 and 27 appears in the two northern regions. In contrast, the deepening rate of isopycnals 26 and 27 in the southern regions is similar. Note that at mooring D, the estimated deepening rate of isopycnal 27 is larger than isopycnal 26 ($2.8 \pm 1.2 > 1.2 \pm 1.4$) but with relatively large uncertainties. We attribute the different deepening rates of isopycnals in the northern basin to the changing pathway of PWW; that is, more PWW is transported to the northern basin at the northern edge of BG, which is revealed in section 3.2.

3.2. PWW Circulation in the Western Arctic Ocean

What is the basin-scale circulation of PWW and its interannual variability in the western Arctic Ocean? A general anticyclonic PWW circulation during 2003–2016 is shown in Figure 7. The depth-averaged velocity in 100–200 m shows similar circulation pattern (Zhao et al., 2018). Mooring B is dominated by a northeastward current, mooring C southeastward current, and mooring D southwestward current, while mooring A does not show a clear preference of current direction likely because it is close to the center of BG (which is revealed in the following discussion of freshwater content distribution). This general anticyclonic circulation of PWW is consistent with the pulse-like signals of PWW advection and the time lag of PWW thickness/freshwater content changes among moorings B, C, and D described in section 3.1.
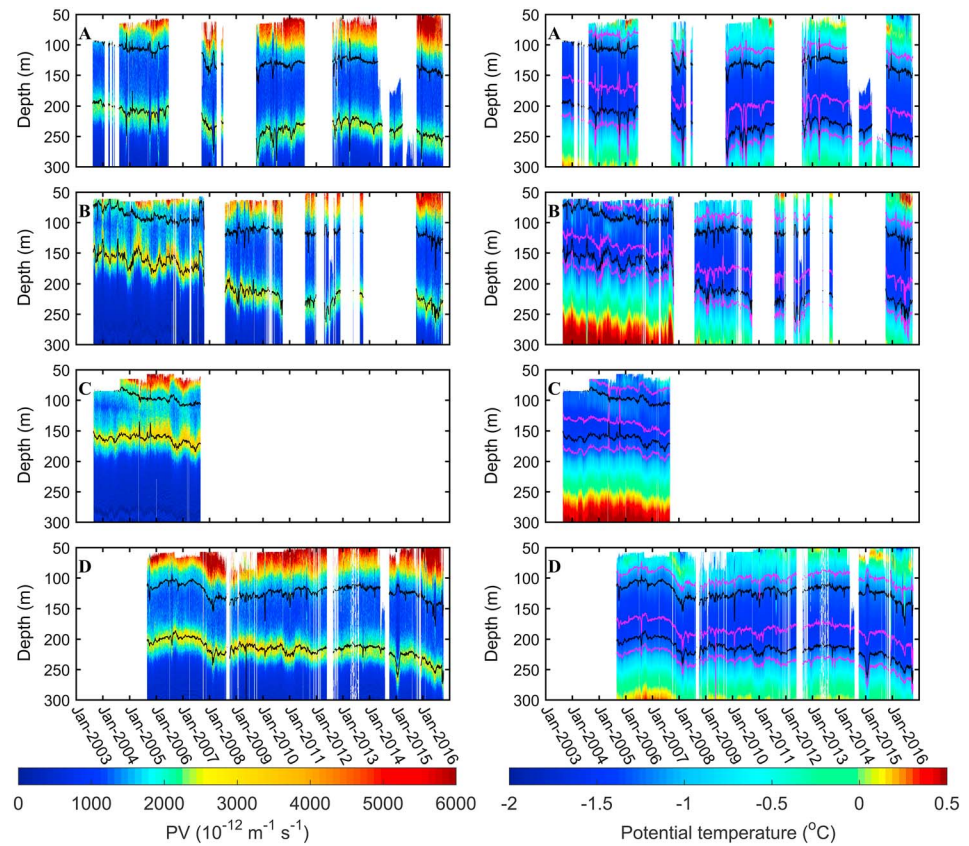
Figure 5. (left column) Potential vorticity (PV) and (right column) potential temperature for moorings A, B, C, and D in 2003–2016 (the white area indicates data gaps). The black lines are the isopycnals 26 and 27 kg/m^3, while the pink lines on the right panels denote salinities 32, 33, and 34.

Another way to look at PWW circulation is by analyzing PV and Montgomery function distribution in the PWW core at isopycnal 26.5 kg/m^3, similar to the studies of subtropical mode water circulation (e.g., Marshall et al., 2001; Marshall & Nurser, 1992; Maze & Marshall, 2011). Based on the interannual variability of geostrophic current in the BG (Zhong et al., 2018), we divided the years 2002–2016 into three periods (i.e., 2002–2006 before the BG spins up, 2007–2010 when the BG spins up, and 2011–2016 when the BG stabilized). The core of the PWW is characterized by low-PV water (Figure 8, upper panels). The low-PV PWW is mainly in the central and southern Canada Basin in 2002–2006, with high PV in the northern basin. This high PV water is an expression of strong stratification between PWW and the deeper AW. In the following period (2007–2010) the low-PV PWW water extends to the northwestern basin, while the southeastern basin is replaced by relative high PV water, and by 2011–2016, almost all the basin is filled with low-PV PWW. As a confirmation of our results, we find similar spatial pattern changes (Figure S6) using a more traditional definition of PWW (i.e., potential temperature at salinity 33.1). To more explicitly trace the movement of PWW, the geostrophic current on the 26.5 kg/m^3 isopycnal is computed from the lateral gradient of Montgomery function (Figure 8, lower panels). The geostrophic current is relatively strong in 2002–2006 along the Northwind Ridge, and it strengthens along the Chukchi Slope as the BG moves to the west in the last two periods (the westward shift of the BG is revealed in Armitage et al., 2017; Zhong et al., 2018). This circulation scheme is similar to the passive tracer trajectory from the model in Timmermans et al. (2017, their Figure S3b).

Results in section 3.1 suggest a different change in the upper halocline compared with the lower halocline. We now describe the multiyear changes of freshwater content in the upper 50 m versus that in the PWW layer, in order to reveal the potential connection between the wind-driven Ekman layer and the PWW circulation. Figure 9 shows that the freshwater content in the upper 50 m is different from that in the PWW layer (upper panels and middle panels) not only in magnitude but also the position of freshwater
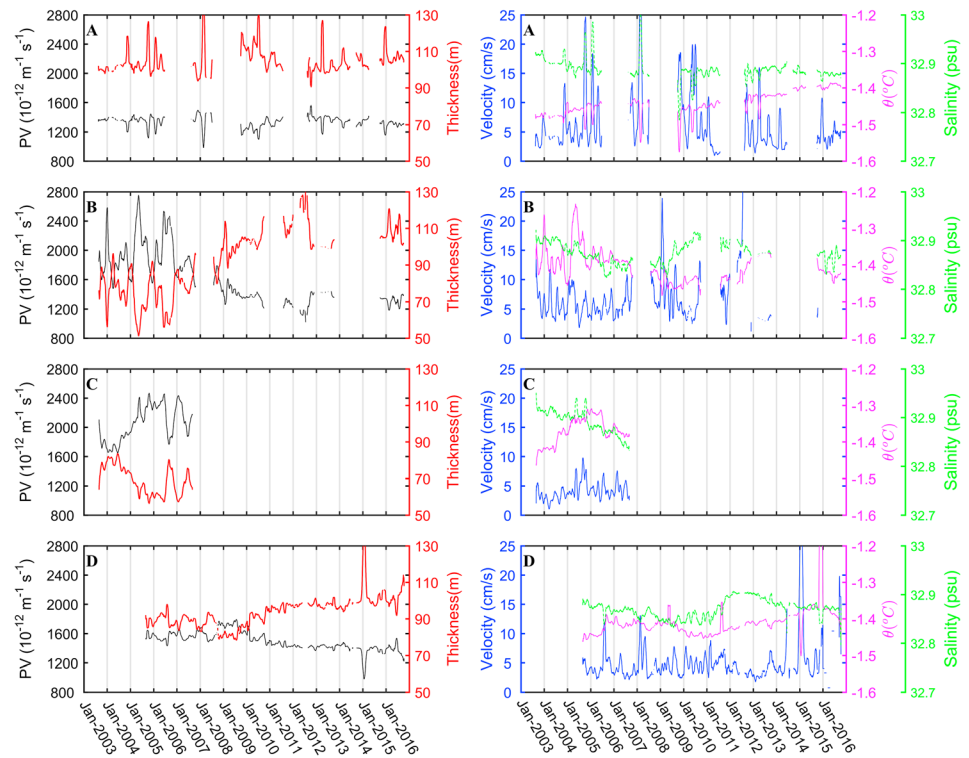
Figure 6. The thickness of the Pacific Winter Water (PWW) layer and average (left column) potential vorticity (PV) and (right column) average velocity, potential temperature and salinity in the PWW layer for moorings A, B, C, and D in 2003–2016. The discontinuous lines indicate data gaps in the mooring records. The original data have been filtered with a 1-month boxcar average (with 29 data points).

content maxima. The freshwater content significantly increases in the last two periods in the upper 50 m, while only a moderate increase is observed in the PWW layer. In particular, the PWW freshwater content shows a redistribution in 2007–2010 from the southern basin to the western basin and Chukchi Borderland, in contrast to that in the upper 50 m. The general implication of this difference is that while both layers moved westward, the PWW moved much further into the Chukchi Borderland or adjacent to the Northwind Ridge. In the upper 50 m, ocean circulation is mainly driven by the Ekman dynamics (Ekman pumping and Ekman transport) and sea surface height gradients. The position shift of the freshwater center of this layer is related to the position shift of Beaufort High center (see Figures 7d–7f in Zhang et al., 2016). The spatial patterns of PWW thickness are consistent with the spatial patterns of freshwater content in the PWW layer (middle panels and lower panels in Figure 9). Both the freshwater content and thickness of the PWW layer show a dramatic basin-scale increase in 2011–2016, with thickness increasing from 76.4 ± 1.2 m to 82.2 ± 0.4 m to 94.7 ± 0.7 m over the three periods.

Table 1
The Annual Deepening Rate of Isopycnals 26 and 27 at Four Defined Regions of the Canada Basin (see Figure 1 for the Regions) From the In Situ Hydrographic Data and Mooring Data During 2002–2016 (Unit: m/year)

Isopycnals (kg/m^3)	Data	Southwest/A	Northwest/B	Northeast/C	Southeast/D
26	in situ hydro	3.6 ± 0.8	3.6 ± 0.7	1.8 ± 0.9	2.4 ± 1.1
	moorings	3.0 ± 1.2	4.1 ± 1.0	—[a]	1.2 ± 1.4
27	in situ hydro	3.3 ± 0.9	6.2 ± 1.3	4.7 ± 1.1	2.4 ± 0.9
	moorings	3.2 ± 1.5	7.6 ± 1.6	—	2.8 ± 1.2

Note. The 95% confidence intervals are used for the linear fit trend.
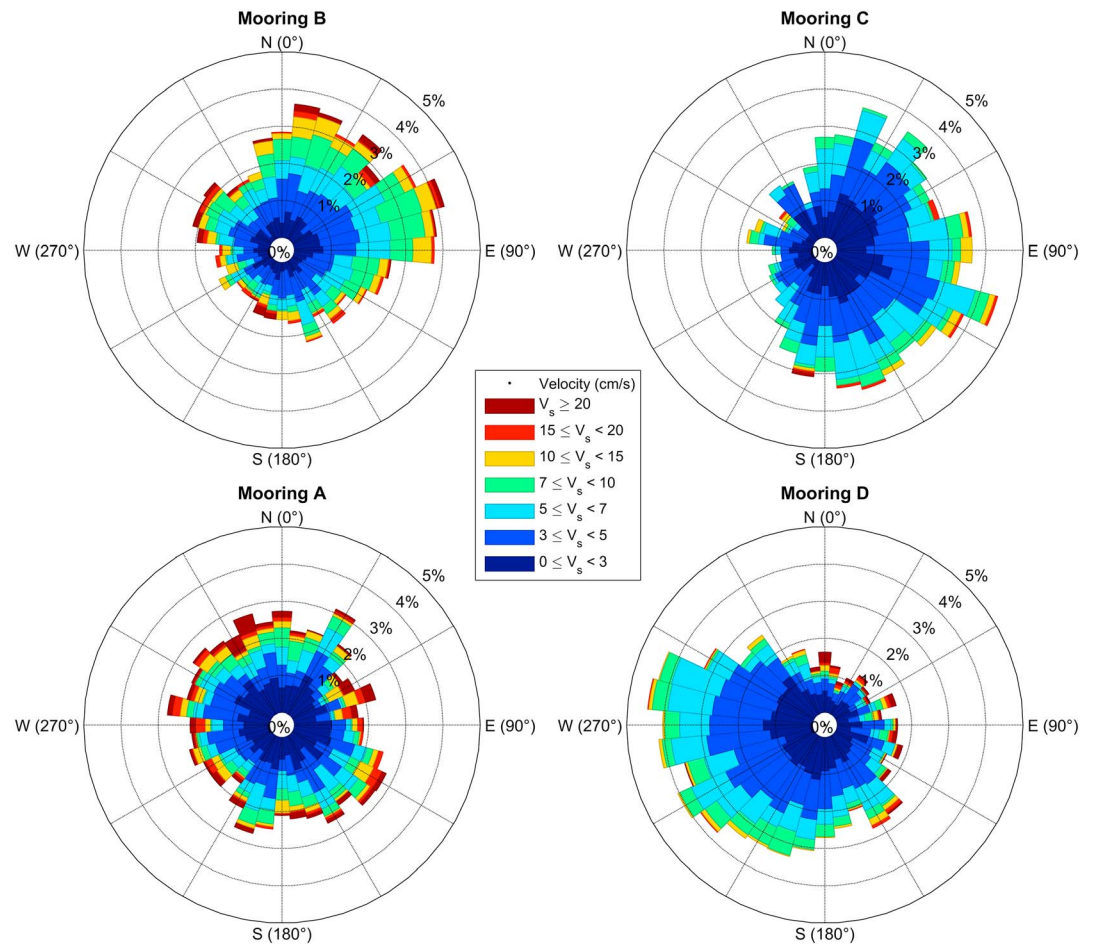[a]Due to the lack of enough measurements at mooring C, no deepening rates are estimated.

Figure 7. Current rose of average velocity in the Pacific Winter Water (PWW) layer from four moorings in 2003–2016 (mooring locations are shown in Figure 1). The frequency count for velocity is marked as percentage.

The total PWW volume in the BG region of period 1 (2002–2006), period 2 (2007–2010), and period 3 (2011–2016) are $3.48 \pm 0.04 \times 10^{14}$ m³, $3.59 \pm 0.01 \times 10^{14}$ m³, and $4.11 \pm 0.02 \times 10^{14}$ m³, respectively (results from lower panels in Figure 9). Over the years from 2002 to 2016, the total PWW volume has increased about 6.33×10^{13} m³ or a net volume increase of 18%. The residence time of PWW in the Canada Basin is estimated to be ~10 years (Ekwurzel et al., 2001; Macdonald et al., 2005). The simulations of a high-resolution model (5 km over the Chukchi Sea) suggest that the movement of Pacific water is strongly constrained by the topography and largely flows through the Barrow Canyon to form the westward flowing Chukchi Slope Current when the BG spins up (Spall et al., 2018). Assuming that all of the deep basin PWW originates from the Chukchi Slope Current, then if its volume transport is ~0.35 Sv (estimated by Corlett & Pickart, 2017) and is sustained at this amplitude throughout the study periods, it would take about $6.33 \times 10^{13}/(0.35 \times 10^{6})/(24 \times 3600 \times 365) \approx 5.7$ years for the deep basin PWW volume to increase from periods 1 to 3 (assuming also that there is no significant PWW outflow from our study region during this time period). This value of 5.7 years is consistent with the time difference between periods 1 and 3.

3.3. Deepening of the Lower Halocline From Ekman Pumping Versus From Lateral Flux Convergence of PWW

In this section, we examine the physical drivers that cause the deepening of the lower halocline in the deep basin. We focus in particular on the depth of the PWW lower bound and consider only the area downstream of the northern Chukchi Sea (where PWW is formed by subduction of shelf water; Timmermans et al., 2017). In the deep basin, the lower halocline can deepen via (i) Ekman pumping or (ii) lateral flux convergence of
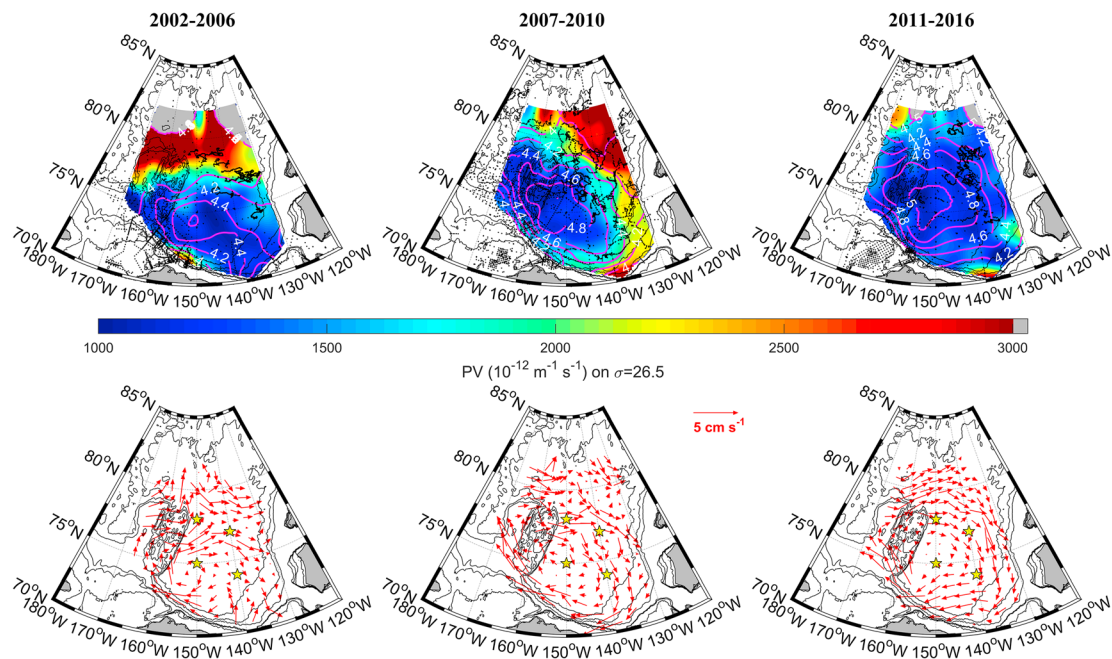
Figure 8. Upper panels: The potential vorticity (PV; shading) on the isopycnal of 26.5 kg/m^3, which represents the core of PWW in three periods. The Montgomery function (with a reference pressure of 1,000 db) is shown as the pink contours, ranging from 3.8 to 5 m^2/s^2 at an interval of 0.2 m^2/s^2. The locations of the hydrographic stations are marked by black dots, and the shading values between the stations are interpolated. The grey areas correspond to grid cells with relative interpolation errors larger than 15%. Lower panels: Geostrophic current (vectors) derived from the Montgomery function in upper panels on the isopycnal of 26.5 kg/m^3. The locations of four Beaufort Gyre Observing System (BGOS) moorings are marked by yellow stars.

PWW. The latter can result from changes in mean advective pathways of PWW or lateral injection of PWW from the Chukchi Sea or from increased lateral eddy flux at depths of PWW. The contribution from advection/injection of PWW is difficult to quantify due to the lack of data, but instead the contribution from lateral eddy flux can be quantified by considering lateral eddy diffusivity as discussed below.

Observationally based estimates of eddy diffusivity in the BG show that it decays with depth over a range of more than 600 m^2/s in the upper layer down to 100 m^2/s below (Meneghello et al., 2017). Here we reprocess the calculation of isopycnal eddy diffusivity using the mooring data by applying mixing length theory (Figure 10), using methods developed in Cole et al. (2015) and Meneghello et al. (2017). Note that eddy diffusivity here is defined as the fluctuations from a mean state with timescales between 1 month and 1 year (i.e., the timescale we used to smooth the mooring data in section 3.2). A brief description of this calculation is provided in Text S1 in the supporting information. The eddy diffusivity here has some differences compared with the results in Meneghello et al. (2017) because of the use of a 1° spatial gradient instead of a 100-km spatial gradient. Additionally, as the details of the upper few hundred meters are the focus of this paper, we adjusted the depth of a single maxima (at the depth range of 100–200 m) in the MIMOC temperature gradient at mooring B upward by 35 m to match the depth of temperature fluctuations observed at this mooring. This adjustment reconciled the difference between the MIMOC climatology data and the mooring data regarding the core of PWW.

The eddy diffusivity is different among different moorings at the depth of 100–200 m, which is dominated by the PWW (Figure 10). All moorings except mooring D show a clear maximum of eddy diffusivity over depths 100–200 m. The largest peaks of eddy diffusivity appear at moorings A and B, followed by C and D (Figure 10c). If the depth of halocline in the BG is only determined by the balance between the Ekman pumping and the corresponding lateral eddy diffusivity (Manucharyan et al., 2016; Manucharyan & Spall, 2016), then the isopycnal slope would be depth-invariant (i.e., isopycnals are parallel, also discussed in Kenigson et al., 2018). Instead, results in Figure 2b revealed that the slope of the isopycnals becomes steeper with depth near the Chukchi Slope (at the edge of BG), which was also noted by Kenigson et al. (2018) using PHC data. Additional evidence is shown in Table 1 that at moorings B and C, there is a significantly different deepening rate of the isopycnals 26 and 27, which also does not correspond to the depth-invariant isopycnal
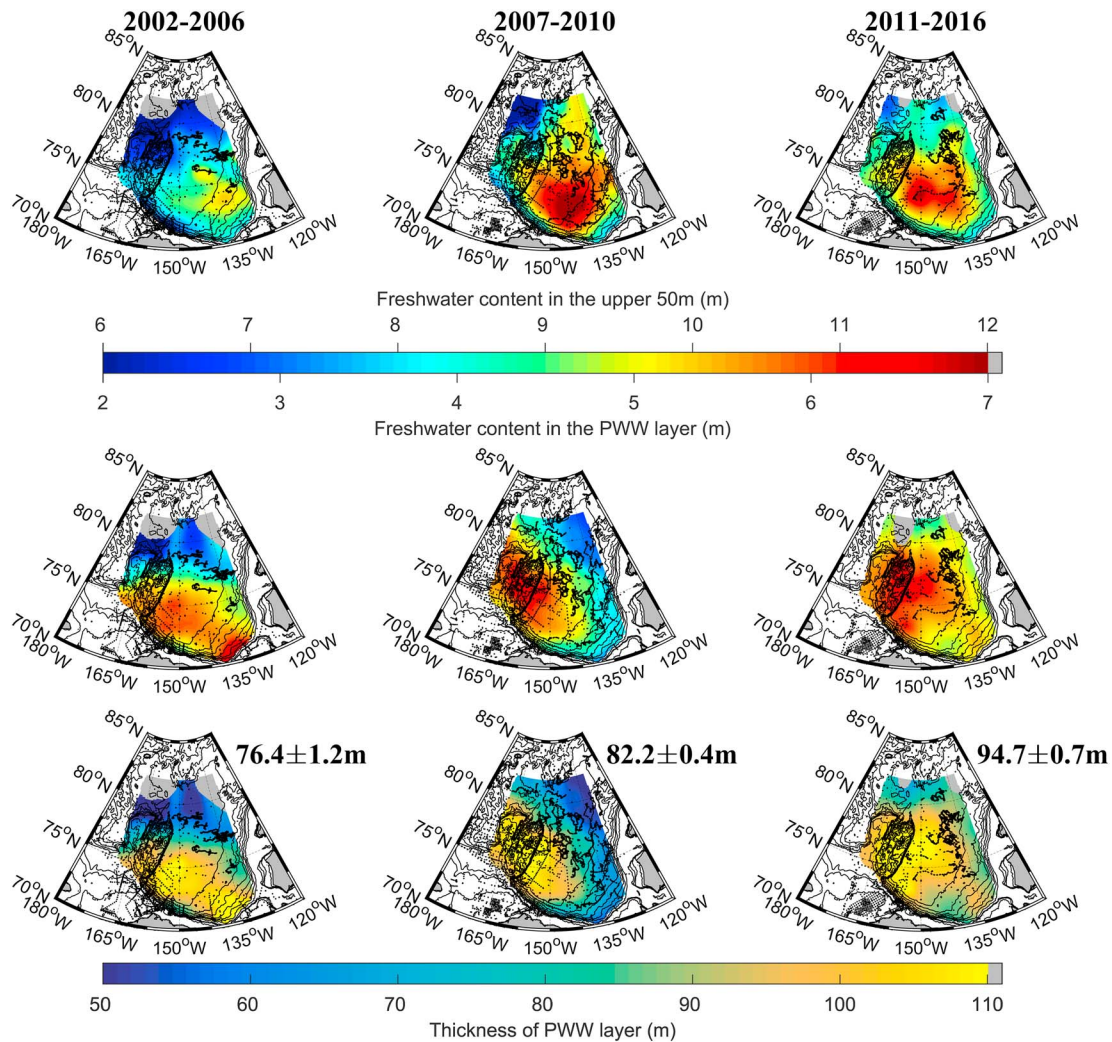
Figure 9. Freshwater content in the (upper panels) upper 50 m versus in the (middle panels) PWW layer relative to the salinity of 34.8 and the thickness of the (lower panels) PWW layer in three periods (different column for the different period). Note that the different ranges of the freshwater content color bar in the upper 50 m versus in the PWW layer. The numbers in the lower panels are the area mean thickness of PWW with the interpolation errors. The gray areas correspond to grid cells with relative interpolation errors larger than 15%.

slope. Based on the relationship between isopycnal slope and eddy diffusivity (e.g., Manucharyan et al., 2016; Manucharyan & Spall, 2016), the depth-invariant isopycnal slope would correspond to a gradually decrease of lateral eddy diffusivity with depth in the upper 200 m, which is not the case we have in Figure 10c. The peaks of lateral eddy diffusivity over depths 100–200 m are obviously related to the additional lateral advection/injection of PWW, because both the standard deviation of potential temperature and velocity are relatively large at this depth range (Figures 10a and 10b).

We now provide a rough calculation to evaluate the contribution of Ekman pumping to the lower halocline deepening based on previous theoretical studies. Here, we assume that there is no additional lateral advection/injection of PWW over depths 100–200 m, and so replace the eddy diffusivity at this depth range with a constant value (500 m²/s; the black dashed line in Figure 10c). The modified eddy diffusivity is corresponds to the depth-invariant isopycnal slope. Using this constant eddy diffusivity and combined with the residual mean theory (Manucharyan & Spall, 2016; Marshall & Radko, 2003), we can derive the halocline thickness deepening toward the center of the gyre. In this way, the depth of the lower PWW bound (i.e., isopycnal 27) is only determined by the balance between Ekman pumping and the corresponding eddy diffusivity. In a steady state, the residual-mean circulation is vanishingly small (Manucharyan et al., 2016; Manucharyan & Spall, 2016; Marshall & Radko, 2003) and we have
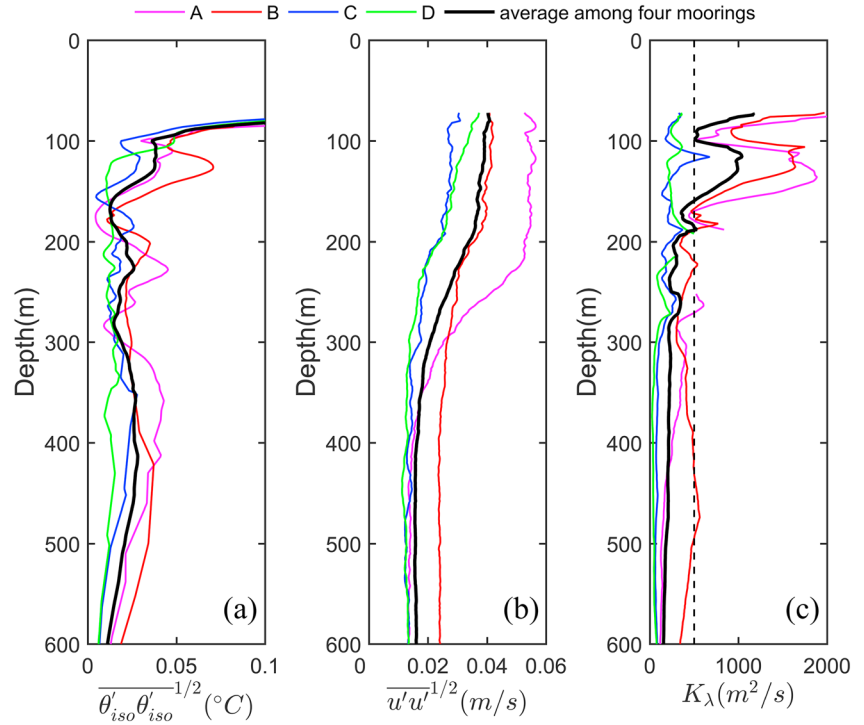
Figure 10. Reprocess of Figure 4 following Meneghello et al. (2017). Profiles of (a) standard deviation of potential temperature θ_{iso}, (b) standard deviation of velocity u, and (c) along-isopycnal eddy diffusivity K_λ at the four moorings. The primed quantities in (a) and (b) represent the fluctuation from the mean. The dashed line represents the value of 500 m²/s. Extrema of mixing lengths at moorings A and D over the depth of 200–250 m are removed and are not used for the diffusivity calculation (see Text S1 in the supporting information for details).

$$\Psi_{\text{res}} = \overline{\Psi} + \Psi^* = 0 \tag{3}$$

where $\overline{\Psi} = \overline{\tau}/(\rho_0 f)$ is the Ekman transport, $\Psi^* = K_D \overline{s}$ is the eddy stream function, K_D is the eddy diffusivity, $\overline{s} = \Delta H/L$ is the isopycnal slope, ΔH is the halocline thickness deepening toward the center of the gyre, and L is the length scale over which the deepening occurs. We then have $\Delta H = \overline{\tau} \cdot L/(\rho_0 f K_D)$; here $\overline{\tau} \cdot L/(\rho_0 f)$ is calculated as an integral of $W_{\text{Ekman}} \cdot dA$ over the central BG area A. Finally, we have

$$\Delta H = \frac{\iint W_{\text{Ekman}} dA}{K_D} \tag{4}$$

where the eddy diffusivity K_D is replaced with K_λ in Figure 10c with a value of 500 m²/s, the Ekman pumping is derived from the combination of air-ocean stress and ice-ocean stress, which are scaled by the sea ice concentration (details in Zhong et al., 2018) and then integrated over a circular area with a radius of 400 km (to simplify the matter, the BG area is represented by a circular area here). The center of the BG is determined by considering the spatial distribution of multiyear mean Ekman pumping and the dynamic ocean topography (Figure S7). We remark that there are uncertainties in the calculation of Ekman pumping (also see Zhong et al., 2018). In the steady state, the halocline deepening at the BG center due to the balance between Ekman pumping and the corresponding eddy diffusivity is $\Delta H = -5.98 \times 10^4 \text{m}^3/\text{s}/500 \text{ m}^2/\text{s} \approx -120$ m.

At mooring B (which has the longest time series and significant different deepening rate of PWW bounds), the hydrographic properties over depths 100–200 m are influenced by the lateral advection of PWW from the Chukchi Borderland (Figure 8). The isopycnal 26 kg/m³ deepens by ~50 m at mooring B during 2003–2011 and then stabilizes in later years, while the isopycnal 27 kg/m³ deepens by ~70 m during 2003–2011 (Figure 5; similar value could obtain from Figure 3a at the northwestern region). The distance between mooring B and the BG center is ~270 km; thus, the halocline deepening at mooring B due to Ekman pumping is (400–270 km) × 120 m/400 km ≈ 40 m based on the slope of halocline (120 m/400 km). This value is

comparable to the deepening of isopycnal 26 kg/m^3 (~50 m) in 2003–2011, which is influenced more by the Ekman pumping (another constraint for this evaluation). Finally, of the 70-m deepening of the lower halocline (isopycnal 27 kg/m^3) observed over 2003–2011, 43% ([70–40 m]/70 m ≈ 43%) resulted from lateral flux convergence of PWW (via lateral advection of PWW from the Chukchi Borderland). Thus, the lateral advection of PWW is an important contribution to the deepening of the lower halocline in the northern Canada Basin (at the edge of BG).

There are many uncertainties of our evaluated K_λ from the mooring data (also see the discussion in Meneghello et al., 2017). For an uncertainty of 20% in K_λ (a reasonable eddy diffusivity could be in the range of 400–600 m^2/s; Manucharyan et al., 2016; Meneghello et al., 2017), this leads to a range of ΔH from −100 to −150 m. The Ekman pumping deepening at mooring B then becomes 33 to 49 m. Then the advection of PWW is responsible for 30 to 53% of the deepening. Presumably, the estimated Ekman pumping also has some error that might widen the range as well. If one uses the variation of isopycnals depth at mooring C for a similar consideration, much smaller lateral advection of PWW will be obtained because mooring C does not cover a long enough time period (i.e., does not cover the rapid deepening period of lower halocline and its stabilization period).

3.4. Potential Influences of the Redistribution of PWW in the Western Arctic Ocean—A Hypothesis for Mesoscale Eddy Formation

The changing pathway of PWW revealed in section 3.2 may influence the formation and distribution of mesoscale eddies in the BG. Ocean velocities larger than 10 cm/s are frequently observed at moorings A and B, suggesting the presence of mesoscale eddies (Figures 7 and 8). Fewer such high-velocity events are found in moorings C and D. Here we study the cold halocline variability (potentially related to the mesoscale eddies formation) by calculating the EAPE (using equation (2)). Figure 11 shows the EAPE at 150-m depth (roughly the core depth of PWW) in three periods. The northern basin and the southern Beaufort shelf are occupied by relatively high EAPE in 2002–2006, which indicates that mesoscale eddies are more likely to form or have formed in these regions compared with the climatological state. Both regions may exhibit baroclinic instability: in the north associated with the front between Pacific and Atlantic *water mass assemblies* (hereafter referred to as the P/A front; McLaughlin et al., 1996) and in the south associated with a strong boundary current (Pickart et al., 2005; Spall et al., 2008; Timmermans et al., 2008). The P/A front is thought to be a source region for double-core eddies, with their shallow cores at the lower halocline (Zhao & Timmermans, 2015). Relatively high EAPE shows a regional shift from the southern basin in 2007–2010 to the western basin and the Chukchi Borderland in 2011–2016, a shift that is coherent with the changing pathway of PWW (Figures 8 and S6). Much higher EAPE in the southern Canada Basin and near the Chukchi Borderland indicates that mesoscale eddies are more likely to form or appear in these regions in the last two periods compared with the climatology field. This evidence suggests that the changing pathway of PWW contributes to the spatial pattern changes of EAPE and its magnitude. The enhanced EAPE either indicates intensified eddy activity or has the potential to result in more eddies. Stronger mesoscale eddy activity would act to homogenize isopycnal PV gradients or reduce the horizontal isopycnal layer thickness gradient. This process occurs at the same time as the PV sources act to increase the thickness, so the two processes counteract each other. Note that some regions filled with *bumps* of high value are actually affected by mesoscale eddies, instead of the *potential ability* to form an eddy. For instance, the relatively high value around 74°N, 145°W (73.5°N, 155°W) in 2007–2010 (2011–2016) indicates that mesoscale eddies already formed in this potentially unstable region. Note also that we do not attempt to estimate the size of mesoscale eddies here, given that length scales in our EAPE fields are strongly influenced by the availability of the in situ profiles and the smoothing techniques we used.

As more freshwater accumulates in the upper Ekman layer and the BG center moves westward (upper panels in Figure 9), this forces PWW entering the basin from the Chukchi Sea to subduct both deeper and farther westward, that is, toward the Chukchi Borderland (Figures 8 and S6). The advection of PWW to the Chukchi Borderland satisfies the criteria for baroclinic instability, as the strong horizontal PV gradient changes sign with depth from the basin to the Chukchi Borderland (Figure 2b and the first period in Figure 8). In this case, the PWW layer is compressed, so that relative vorticity is generated to satisfy PV conservation. This is in contrast to the cross-front flow that compresses water from the Eurasian Water to the Canadian Water, which is described in Zhao and Timmermans (2015). For a water column of the PWW
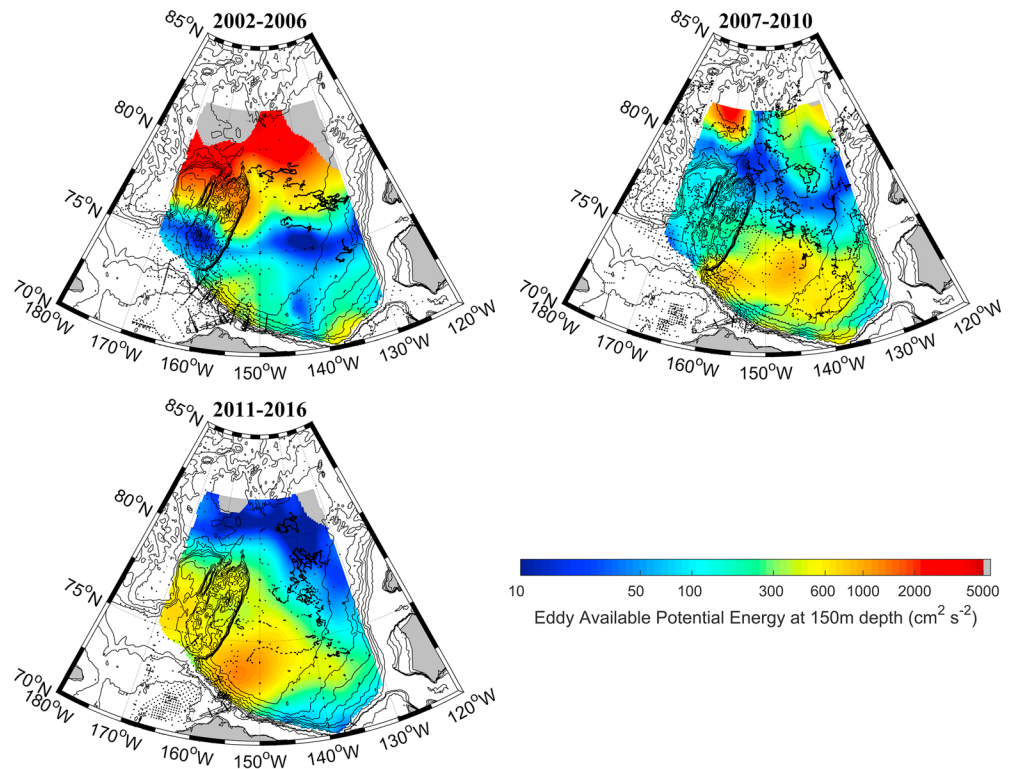
Figure 11. Eddy available potential energy at 150-m depth in three periods using Polar Hydrographic Climatology (PHC) climatology data as the mean state. The black dots are represented as the hydrographic stations, and the values between stations are interpolated. The grey areas correspond to grid cells with relative interpolation errors larger than 15%.

layer initially with zero relative vorticity, the generated relative vorticity is $\zeta_F = f(h_F - h_I)/h_I$, where h_I and h_F are the initial PWW thickness and final thickness, respectively. This formula indicates that the compression of PWW layer as it moves westward could result in the generation of anticyclonic mesoscale eddies, similar to the formation process of deep mesoscale eddies described by Carpenter and Timmermans (2012). We consider an initial PWW thickness of ~100 m at 75°N, 161.5°W that compresses to a thickness of ~65 m at
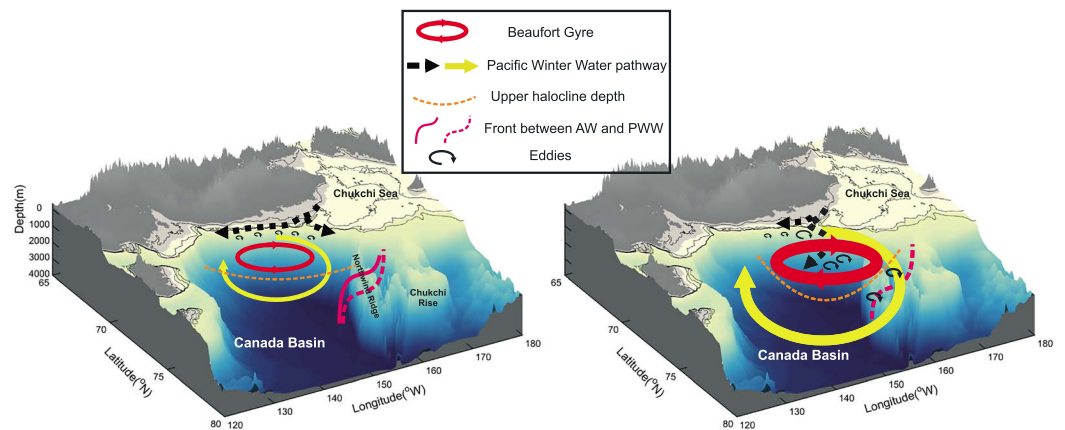

Figure 12. Schematic diagram of the pathway of Pacific Winter Water (PWW) and its connection with the Beaufort Gyre. (left) Early period versus (right) later period. The red circles represent the domain of the Beaufort Gyre (BG). The thick black dashed lines represent boundary currents (PWW inflow), while the yellow lines represent the PWW circulation in the basin. The brown dashed lines represent the depth of upper halocline. The solid and dashed pink lines represent the fronts between Atlantic Water (AW) and PWW in the early period and later period, respectively. The dashed pink line is replicated in the left panel to show the depression of the front in the later period.

75°N, 167°W in Figure 2b (similar values could be derived from the lower panels in Figure 9 for years 2002–2006 in the Chukchi Borderland or from Figure S3). The Rossby number of the resulting mesoscale eddy by this process would be: $R_0 = V/(fR) = \zeta/(2f) = (h_F - h_I)/2h_I \approx 0.18$. For the lower halocline eddies at mooring B (78°N) with a typical maximum rotational velocity of 30 cm/s and a Rossby deformation radius of ~12 km (Zhao et al., 2014; Zhao & Timmermans, 2015), the Rossby number of these mesoscale eddies is $R_0 = V/(fR) = 0.3\text{m/s}/(12\text{km} \times 1.42 \times 10^{-4}/\text{s}) \approx 0.18$. This is consistent with the Rossby number of mesoscale eddies that could be generated by the PWW layer compressed through its advection. Thus, it is reasonable to hypothesize that the lower halocline eddies are formed by the advection of PWW to the frontal region in the Chukchi Borderland.

4. Summary and Discussion

The main objective of this study was to investigate the circulation of PWW in the western Arctic Ocean, focusing on changes occurring downstream from the area where PWW is subducted into the deep basin from the Chukchi Sea. Our analysis of in situ hydrographic data shows that the upper bound of PWW is influenced primarily by Ekman convergence and is deepened at a rate of 3.6 ± 0.7 m/year and 1.8 ± 0.9 m/year during 2002–2016 in the northwestern and northeastern basin, respectively. On the other hand, the lower bound of PWW is influenced by both Ekman convergence and lateral flux convergence of PWW with a deepening rate of 6.2 ± 1.3 m/year and 4.7 ± 1.1 m/year during the same period in the northwestern and northeastern basin, respectively. The influence of lateral flux convergence is most apparent at the northern edge of the BG, where the deepening rate of the lower bound of PWW is almost double that of its upper bound. In contrast, the upper and lower bounds of PWW show a similar deepening rate of 2.4~3.6 m/year near the center of the BG (the southern two regions) because of stronger Ekman pumping and relatively small lateral flux convergence of PWW. We estimate that of the 70-m deepening of the lower bound of PWW (i.e., isopycnal 27 kg/m^3 or lower halocline) observed over 2003–2011 in the northwestern basin, 43% resulted from lateral flux convergence of PWW (via lateral advection of PWW from the Chukchi Borderland). The total PWW volumes in the BG region of period 1 (2002–2006), period 2 (2007–2010), and period 3 (2011–2016) are $3.48 \pm 0.04 \times 10^{14}$ m^3, $3.59 \pm 0.01 \times 10^{14}$ m^3, and $4.11 \pm 0.02 \times 10^{14}$ m^3, respectively. It has increased about 18% over the years. We also find that the PWW is warming in the Canada Basin (Figure 4), likely because its upstream source is warming. The pulse-like warming signals of PWW are evident in the northern and southeastern basin, while PWW shows a linear warming in the southwestern basin. This difference likely arises because the southwestern basin is close to the inflow of PWW from the Chukchi Sea, while the rest of the basin (i.e., the northern and southeastern basin) experiences interannual advection variability of PWW along its pathway. Hydrographic and mooring data revealed that the contribution of lateral flux convergence of PWW to the deepening of the PWW lower bound is only noticeable at the edge of BG (Table 1 and section 3.3), where the magnitude of Ekman pumping is relatively small.

The PWW is another source of freshwater in the BG that originates via subduction from the Chukchi Sea, in contrast to the wind-driven Ekman convergence of surface freshwater. However, these two freshwater sources do have close connections. The Ekman convergence builds up the freshwater dome and deepens the upper halocline; in response, the subduction of relatively dense PWW has to be deeper. Also, the westward movement of the Ekman layer (Figure 9) forces PWW entering the basin from the Chukchi Sea to subduct farther westward to the Chukchi Borderland, resulting in higher EAPE in the halocline (Figure 11). The corresponding eddy diffusivity might change as well, and this remains to be further investigated.

The redistribution of PWW in the basin tends to reduce the asymmetry of the BG in its vertical structure by changing the depth of isopycnals. In this way, a different large-scale circulation in the PWW layer is established. Based on our results, two circulation regimes of PWW are revealed (Figure 12). In the early periods, the boundary current is relatively strong (Brugler et al., 2014), while the BG was weak and the depth of the upper halocline was relatively flat. The P/A front in the Chukchi Borderland was relatively strong and shallow. In the latter periods, the boundary current is relatively weak (Brugler et al., 2014), while the BG is spinning up and the upper BG is shifting to the Chukchi Borderland because of the wind forcing regime shifts. PWW is deepest in the center of the gyre compared to the edges. A shift in the gyre toward the northwest would result in a larger deepening rate observed in the northwest. This might explain the different

deepening rates of the upper PWW bound between the northwestern and northeastern basin. The depth of the upper halocline is increasing due to stronger Ekman pumping and accumulation of freshwater. The inflow of PWW is affected by the depth change of the upper halocline and the sea surface height gradient between the basin and shelf (Spall et al., 2018), so that the pathway of PWW is changing to the northwest toward the Chukchi Borderland (Figure 8). We hypothesized that the compression of the PWW layer between the P/A front and the upper halocline in the Chukchi Borderland could give rise to lower halocline mesoscale eddies and this results in the larger EAPE field (Figure 11). In this way, we explain why there are more lower halocline eddies emerging in the western Canada Basin (Zhao et al., 2016). These lower halocline eddies would flatten the steep isopycnals in the periphery of the BG. This could be a key factor for the recent stabilization of the BG. Our results indicate that the redistribution of PWW is related with the overlaying westward shift of the BG and this redistribution would potentially regulate the expansion and extension of the acidification water in the western Arctic Ocean (Qi et al., 2017).

References

Aagaard, K., Coachman, L., & Carmack, E. (1981). On the halocline of the Arctic Ocean. *Deep Sea Research Part A: Oceanographic Research Papers*, *28*(6), 529–545. https://doi.org/10.1016/0198-0149(81)90115-1

Aksenov, Y., Ivanov, V. V., Nurser, A. J. G., Bacon, S., Polyakov, I. V., Coward, A. C., et al. (2011). The Arctic circumpolar boundary current. *Journal of Geophysical Research*, *116*, C09017. https://doi.org/10.1029/2010JC006637

Aksenov, Y., Karcher, M., Proshutinsky, A., Gerdes, R., de Cuevas, B., Golubeva, E., et al. (2016). Arctic pathways of Pacific water: Arctic Ocean Model Intercomparison experiments. *Journal of Geophysical Research: Oceans*, *121*, 27–59. https://doi.org/10.1002/2015JC011299

Armitage, T. W. K., Bacon, S., Ridout, A. L., Petty, A. A., Wolbach, S., & Tsamados, M. (2017). Arctic Ocean surface geostrophic circulation 2003–2014. *The Cryosphere*, *11*(4), 1767–1780. https://doi.org/10.5194/tc-11-1767-2017

Behrendt, A., Sumata, H., Rabe, B., & Schauer, U. (2018). UDASH—Unified Database for Arctic and Subarctic Hydrography. *Earth System Science Data*, *10*(2), 1119–1138. https://doi.org/10.5194/essd-10-1119-2018

Brugler, E. T., Pickart, R. S., Moore, G. W. K., Roberts, S., Weingartner, T. J., & Statscewich, H. (2014). Seasonal to interannual variability of the Pacific water boundary current in the Beaufort Sea. *Progress in Oceanography*, *127*, 1–20. https://doi.org/10.1016/j.pocean.2014.05.002

Carpenter, J. R., & Timmermans, M.-L. (2012). Deep mesoscale eddies in the Canada Basin, Arctic Ocean. *Geophysical Research Letters*, *39*, L20602. https://doi.org/10.1029/2012GL053025

Coachman, L. K., Aagaard, K., & Tripp, R. B. (1975). *Bering Strait: The regional physical oceanography*, (p. 172). Seattle, Wash: Univ. of wash. Press.

Codispoti, L. A., Flagg, C., & Kelly, V. (2005). Hydrographic conditions during the 2002 SBI process experiments. *Deep Sea Research, Part II*, *52*(24-26), 3199–3226. https://doi.org/10.1016/j.dsr2.2005.10.007

Cole, S. T., Wortham, C., Kunze, E., & Owens, W. B. (2015). Eddy stirring and horizontal diffusivity from Argo float observations: Geographic and depth variability. *Geophysical Research Letters*, *42*, 3989–3997. https://doi.org/10.1002/2015GL063827

Corlett, W., & Pickart, R. S. (2017). The Chukchi Slope Current. *Progress in Oceanography*, *153*, 50–65. https://doi.org/10.1016/j.pocean.2017.04.005

Dewey, S., Morison, J., Kwok, R., Dickinson, S., Morison, D., & Andersen, R. (2018). Arctic ice-ocean coupling and gyre equilibration observed with remote sensing. *Geophysical Research Letters*, *45*, 1499–1508. https://doi.org/10.1002/2017GL076229

Ekwurzel, B., Schlosser, P., Mortlock, R. A., Fairbanks, R. G., & Swift, J. H. (2001). River runoff, sea ice meltwater, and Pacific water distribution and mean residence times in the Arctic Ocean. *Journal of Geophysical Research*, *106*(C5), 9075–9092. https://doi.org/10.1029/1999JC000024

Itoh, M., Shimada, K., Kamoshida, T., McLaughlin, F., Carmack, E., & Nishino, S. (2012). Interannual variability of PWW inflow through Barrow Canyon from 2000 to 2006. *Journal of Oceanography*, *68*(4), 575–592. https://doi.org/10.1007/s10872-012-0120-1

Jakobsson, M., Mayer, L., Coakley, B., Dowdeswell, J. A., Forbes, S., Fridman, B., et al. (2012). The International Bathymetric Chart of the Arctic Ocean (IBCAO) version 3.0. *Geophysical Research Letters*, *39*, L12609. https://doi.org/10.1029/2012GL052219

Jones, E. P., & Anderson, L. G. (1986). On the origin of the chemical properties of the Arctic Ocean halocline. *Journal of Geophysical Research*, *91*(C9), 10,759–10,767. https://doi.org/10.1029/JC091iC09p10759

Kenigson J. S., Gelderloos, R., & Manucharyan, G. E. (2018). Role of eddies in shaping the vertical structure of the Beaufort Gyre halocline and its geostrophic circulation, Ocean Science Meeting 2018, Portland, Oregon, USA, [Available online at https://agu.confex.com/agu/os18/meetingapp.cgi/Paper/314222]

Krishfield, R., Toole, J., Proshutinsky, A., & Timmermans, M.-L. (2008). Automated ice-tethered profilers for seawater observations under pack ice in all seasons. *Journal of Atmospheric and Oceanic Technology*, *25*(11), 2091–2105. https://doi.org/10.1175/2008JTECHO587.1

Lique, C., Guthrie, J. D., Steele, M., Proshutinsky, A., Morison, J. H., & Krishfield, R. (2014). Diffusive vertical heat flux in the Canada Basin of the Arctic Ocean inferred from moored instruments. *Journal of Geophysical Research: Oceans*, *119*, 496–508. https://doi.org/10.1002/2013JC009346

Luecke, C. A., Arbic, B. K., Bassette, S. L., Richman, J. G., Shriver, J. F., Alford, M. H., et al.. (2017). The global mesoscale eddy available potential energy field in models and observations. *Journal of Geophysical Research: Oceans*, *122*, 9126, 9143. https://doi.org/10.1002/2017JC013136

Macdonald, R. W., Harner, T., & Fyfe, J. (2005). Recent climate change in the Arctic and its impact on contaminant pathways and interpretation of temporal trend data. *Science of The Total Environment*, *342*(1-3), 5–86. https://doi.org/10.1016/j.scitotenv.2004.12.059

Manucharyan, G. E., & Spall, M. A. (2016). Wind-driven freshwater buildup and release in the Beaufort Gyre constrained by mesoscale eddies. *Geophysical Research Letters*, *43*, 273–282. https://doi.org/10.1002/2015GL065957

Manucharyan, G. E., Spall, M. A., & Thompson, A. F. (2016). A theory of the wind-driven Beaufort Gyre variability. *Journal of Physical Oceanography*, *46*(11), 3263–3278. https://doi.org/10.1175/JPO-D-16-0091.1

Marshall, J., Nilsson, J., & Jamous, D. (2001). Entry, flux, and exit of potential vorticity in ocean circulation. *Journal of Physical Oceanography*, *31*(3), 777–789. https://doi.org/10.1175/1520-0485(2001)031<0777:EFAEOP>2.0.CO;2

Marshall, J., & Nurser, J. G. (1992). Fluid dynamics of oceanic thermocline ventilation. *Journal of Physical Oceanography*, *22*(6), 583–595. https://doi.org/10.1175/1520-0485(1992)022<0583:FDOOTV>2.0.CO;2

Marshall, J., & Radko, T. (2003). Residual-mean solutions for the Antarctic circumpolar current and its associated overturning circulation. *Journal of Physical Oceanography*, *33*(11), 2341–2354. https://doi.org/10.1175/1520-0485(2003)033<2341:RSFTAC>2.0.CO;2

Maze, G., & Marshall, J. (2011). Diagnosing the observed seasonal cycle of Atlantic subtropical mode water using potential vorticity and its attendant theorems. *Journal of Physical Oceanography*, *41*(10), 1986–1999. https://doi.org/10.1175/2011JPO4576.1

McDougall, T. J. (1989). Streamfunctions for the lateral velocity vector in a compressible ocean. *Journal of Marine Research*, *47*(2), 267–284. https://doi.org/10.1357/002224089785076271

McLaughlin, F. A., Carmack, E. C., Macdonald, R. W., & Bishop, J. K. B. (1996). Physical and geochemical properties across the Atlantic/Pacific water mass front in the southern Canadian Basin. *Journal of Geophysical Research*, *101*(C1), 1183–1197. https://doi.org/10.1029/95JC02634

McLaughlin, F. A., Carmack, E. C., Williams, W. J., Zimmermann, S., Shimada, K., & Itoh, M. (2009). Joint effects of boundary currents and thermohaline intrusions on the warming of Atlantic Water in the Canada Basin, 1993–2007. *Journal of Geophysical Research*, *114*, C00A12. https://doi.org/10.1029/2008JC005001

McPhee, M. G. (2013). Intensification of geostrophic currents in the Canada Basin, Arctic Ocean. *Journal of Climate*, *26*(10), 3130–3138. https://doi.org/10.1175/JCLI-D-12-00289.1

Melling, H. (1993). The formation of a haline shelf front in wintertime in an ice-covered Arctic Sea. *Continental Shelf Research*, *13*(10), 1123–1147. https://doi.org/10.1016/0278-4343(93)90045-Y

Melling, H., & Lewis, E. (1982). Shelf drainage flows in the Beaufort Sea and their effect on the Arctic Ocean pycnocline. *Deep Sea Research Part A*, *29*(8), 967–985. https://doi.org/10.1016/0198-0149(82)90021-8

Meneghello, G., Marshall, J., Cole, S. T., & Timmermans, M.-L. (2017). Observational inferences of lateral eddy diffusivity in the halocline of the Beaufort Gyre. *Geophysical Research Letters*, *44*, 12,331–12,338. https://doi.org/10.1002/2017GL075126

Meneghello, G., Marshall, J., Timmermans, M., & Scott, J. (2018). Observations of seasonal upwelling and downwelling in the Beaufort Sea mediated by sea ice. *Journal of Physical Oceanography*, *48*(4), 795–805. https://doi.org/10.1175/JPO-D-17-0188.1

Nishino, S., Shimada, K., Itoh, M., Yamamoto-Kawai, M., & Chiba, S. (2008). East–west differences in water mass, nutrient, and chlorophyll a distributions in the sea ice reduction region of the western Arctic Ocean. *Journal of Geophysical Research*, *113*, C00A01. https://doi.org/10.1029/2007JC004666

Pickart, R., Weingartner, T., Pratt, L., Zimmermann, S., & Torres, D. (2005). Flow of winter transformed Pacific water into the Western Arctic. *Deep Sea Research*, *52*(24-26), 3175–3198. https://doi.org/10.1016/j.dsr2.2005.10.009

Proshutinsky, A., Krishfield, R., Timmermans, M.-L., Toole, J., Carmack, E., McLaughlin, F., et al. (2009). Beaufort Gyre freshwater reservoir: State and variability from observation. *Journal of Geophysical Research*, *114*, C00A10. https://doi.org/10.1029/2008JC005104

Proshutinsky, A., Timmermans, M.-L., Ashik, I., Beszczynska-Moeller, A., Carmack, E., Frolov, I., et al. (2011). The Arctic (ocean) [in "State of the climate in 2010"]. *Bulletin of the American Meteorological Society*, *92*(6), S145–S148.

Qi, D., Chen, L., Chen, B., Gao, Z., Zhong, W., Feely, R. A., et al. (2017). Increase in acidifying water in the western Arctic Ocean. *Nature Climate Change*, *7*(3), 195–199. https://doi.org/10.1038/nclimate3228

Schmidtko, S., Johnson, G. C., & Lyman, J. M. (2013). MIMOC: A global monthly isopycnal upper-ocean climatology with mixed layers. *Journal of Geophysical Research: Oceans*, *118*, 1658–1672. https://doi.org/10.1002/jgrc.20122

Shimada, K., Itoh, M., Nishino, S., McLaughlin, F., Carmack, E., & Proshutinsky, A. (2005). Halocline structure in the Canada Basin of the Arctic Ocean. *Geophysical Research Letters*, *32*, L03605. https://doi.org/10.1029/2004GL021358

Spall, M., Pickart, R., Fratantoni, P., & Plueddemann, A. (2008). Western Arctic shelfbreak eddies: Formation and transport. *Journal of Physical Oceanography*, *38*(8), 1644–1668. https://doi.org/10.1175/2007JPO3829.1

Spall, M. A., Pickart, R. S., Li, M., Itoh, M., Lin, P., Kikuchi, T., & Qi, Y. (2018). Transport of Pacific water into the Canada Basin. *Journal of Geophysical Research: Oceans*, *123*, 7453–7471. https://doi.org/10.1029/2018JC013825

Steele, M., & Boyd, T. (1998). Retreat of the cold halocline layer in the Arctic Ocean. *Journal of Geophysical Research*, *103*(C5), 10419–10435. https://doi.org/10.1029/98JC00580

Steele, M., Morison, J., Ermold, W., Rigor, I., Ortmeyer, M., & Shimada, K. (2004). Circulation of summer Pacific halocline water in the Arctic Ocean. *Journal of Geophysical Research*, *109*, C02027. https://doi.org/10.1029/2003JC002009

Steele, M., Morley, R., & Ermold, W. (2001). PHC: A global ocean hydrography with a high-quality Arctic Ocean. *Journal of Climate*, *14*(9), 2079–2087. https://doi.org/10.1175/1520-0442(2001)014<2079:PAGOHW>2.0.CO;2

Swift, J. H. (2017). HLY1502, data file 320620140320_hy1.csv, CLIVAR and Carbon Hydrographic Data Office, La Jolla, CA, USA.

Timmermans, M.-L., Marshall, J., Proshutinsky, A., & Scott, J. (2017). Seasonally derived components of the Canada Basin halocline. *Geophysical Research Letters*, *44*, 5008–5015. https://doi.org/10.1002/2017GL073042

Timmermans, M.-L., Proshutinsky, A., Golubeva, E., Jackson, J. M., Krishfield, R., McCall, M., et al. (2014). Mechanisms of Pacific Summer Water variability in the Arctic's Central Canada Basin. *Journal of Geophysical Research: Oceans*, *119*, 7523–7548. https://doi.org/10.1002/2014JC010273

Timmermans, M.-L., Toole, J., Proshutinsky, A., Krishfield, R., & Plueddemann, A. (2008). Eddies in the Canada Basin, Arctic Ocean, observed from ice-tethered profilers. *Journal of Physical Oceanography*, *38*(1), 133–145. https://doi.org/10.1175/2007JPO3782.1

Toole, J. M., Krishfield, R. A., Timmermans, M.-L., & Proshutinsky, A. (2011). The ice-tethered profiler: Argo of the arctic. *Oceanography*, *24*(3), 126–135. https://doi.org/10.5670/oceanog.2011.64

Troupin, C., Barth, A., Sirjacobs, D., Ouberdous, M., Brankart, J.-M., Brasseur, P., et al. (2012). Generation of analysis and consistent error fields using the Data Interpolating Variational Analysis (DIVA). *Ocean Modelling*, *52-53*, 90–101. https://doi.org/10.1016/j.ocemod.2012.05.002

Weingartner, T. J., Cavalieri, D. J., Aagaard, K., & Sasaki, Y. (1998). Circulation, dense water formation, and outflow on the northeast Chukchi Shelf. *Journal of Geophysical Research*, *103*(C4), 7647–7661. https://doi.org/10.1029/98JC00374

Woodgate, R. A., & Aagaard, K. (2005). Revising the Bering Strait freshwater flux into the Arctic Ocean. *Geophysical Research Letters*, *32*, L02602. https://doi.org/10.1029/2004GL021747

Woodgate, R. A., Aagaard, K., Swift, J. H., Falkner, K. K., & Smethie, W. M. (2005). Pacific ventilation of the Arctic Ocean's lower halocline by upwelling and diapycnal mixing over the continental margin. *Geophysical Research Letters*, *32*, L18609. https://doi.org/10.1029/2005GL023999

Woodgate, R. A., Aagaard, K., & Weingartner, T. (2005). A year in the physical oceanography of the Chukchi Sea: Moored measurements from autumn 1990–1991. *Deep-Sea Research Part II*, *52*(24-26), 3116–3149. https://doi.org/10.1016/j.dsr2.2005.10.016

Yang, J., Proshutinsky, A., & Lin, X. (2016). Dynamics of an idealized Beaufort Gyre: 1. The effect of a small beta and lack of western boundaries. *Journal of Geophysical Research: Oceans*, *121*, 1249–1261. https://doi.org/10.1002/2015JC011296

Zhang, J., Steele, M., Runciman, K., Dewey, S., Morison, J., Lee, C., et al. (2016). The Beaufort Gyre intensification and stabilization: A model-observation synthesis. *Journal of Geophysical Research: Oceans*, *121*, 7933–7952. https://doi.org/10.1002/2016JC012196

Zhao, M., & Timmermans, M.-L. (2015). Vertical scales and dynamics of eddies in the Arctic Ocean's Canada Basin. *Journal of Geophysical Research: Oceans*, *120*, 8195–8209. https://doi.org/10.1002/2015JC011251

Zhao, M., Timmermans, M.-L., Cole, S., Krishfield, R., Proshutinsky, A., & Toole, J. (2014). Characterizing the eddy field in the Arctic Ocean halocline. *Journal of Geophysical Research: Oceans*, *119*, 8800–8817. https://doi.org/10.1002/2014JC010488

Zhao, M., Timmermans, M.-L., Cole, S., Krishfield, R., & Toole, J. (2016). Evolution of the eddy field in the Arctic Ocean's Canada Basin, 2005–2015. *Geophysical Research Letters*, *43*, 8106–8114. https://doi.org/10.1002/2016GL069671

Zhao, M., Timmermans, M.-L., Krishfield, R., & Manucharyan, G. (2018). Partitioning of kinetic energy in the Arctic Ocean's Beaufort Gyre. *Journal of Geophysical Research: Oceans*, *123*, 4806–4819. https://doi.org/10.1029/2018JC014037

Zhong, W., Steele, M., Zhang, J., & Zhao, J. (2018). Greater role of geostrophic currents in Ekman dynamics in the western Arctic Ocean as a mechanism for Beaufort Gyre Stabilization. *Journal of Geophysical Research: Oceans*, *123*, 149–165. https://doi.org/10.1002/2017JC013282